Preprints (www.preprints.org) | NOT PEER-REVIEWED | Posted: 17 June 2022 doi:10.20944/preprints202206.0251.v1

Contextual accuracy assessments for InSAR methods using synthetic data

Kelly M. Olsen[a,*], Matthew T. Calef[a], Piyush S. Agram[a]

[a] *Descartes Labs, 1607 Paseo de Peralta, Suite B, Santa Fe, NM, 87501, USA*

*Corresponding author

Email addresses: kelly.olsen@descarteslabs.com (Kelly M. Olsen), mattcale@descarteslabs.com (Matthew T. Calef), piyush@descarteslabs.com (Piyush S. Agram)

 doi:10.20944/preprints202206.0251.v1

Abstract

InSAR and associated analytic methods enable relative surface deformation measurements from low Earth orbit with a potential accuracy of centimeters to millimeters. However, assessing the actual accuracy of individual points can be quite difficult. The analytic methods are complicated enough that naïve analytic error propagation is infeasible, and, in many settings, InSAR practitioners lack sufficient ground truth to assess results. Phase noise due to partial decorrelation from changes in the scattering properties of the ground is a prominent source of accuracy loss. In this paper we present a method to assess the loss of precision due to this component of phase noise. The proposed method consists of generating synthetic data whose statistical properties match that of the actual input SAR data stacks, and then using the synthetic data for an ensemble calculation. The spread of the results of the ensemble calculation indicates the loss of precision. We show examples of the ensemble analysis at a mining operation in South Africa, and demonstrate the ability to assess the most reliable methods for particular points of interest using this ensemble analysis and the ability to filter out points based on the width of the spread of results.

Keywords: InSAR, deformation, synthetic data, ensemble methods, uncertainty estimate, time series analysis

1. Introduction

Interferometric Synthetic Aperature Radar (InSAR) enables measurements of surface deformation with a potential accuracy of centimeters to millimeters (Rosen et al., 2000). A complex valued Synthetic Aperture Radar (SAR) image consists of pixels whose phase is determined by the scattering properties on the Earth's surface and the effective round trip distance between the satellite and the surface. If the scattering properties change minimally, the phase change between corresponding pixels in two co-registered complex SAR images will reflect changes in the effective round trip distance between the satellite and the surface and can detect surface displacements in the imaged area. Methods such as the Small Baseline Subset (SBAS) method (Berardino et al., 2002), the Permanent Scatterers (PS) method (Ferretti et al., 2001), and their variants can then be used to extract surface deformation from phase differences in a series of complex SAR images.

There are a number of potential sources of error that InSAR methods must address to extract the most accurate surface deformation. First, the effective round trip distance between the satellite and the surface includes effects from tropospheric moisture and free electrons in the ionosphere (Goldstein, 1995; Zebker et al., 1997). Second, successive passes do not revisit the same orbital paths exactly, which can lead to geometrical decorrelation (Rodriguez and Martin, 1992; Zebker and Villasenor, 1992). Third, differences in the actual round-trip distance between the satellite and the ground can be estimated using precise orbit data and a digital elevation model (DEM), but the residual errors are still larger than the deformation one seeks to measure. Fourth, the desired component of the phase is the round trip distance between the satellite and the ground modulo the wavelength, which is a few centimeters, mapped to $[-\pi, \pi)$, see Goldstein et al. (1988). The process of recovering an "absolute" phase from the observed or "wrapped" phase is called *unwrapping*, and without additional constraints the problem is ill-posed. Finally, the scattering properties of the ground change with time, resulting in temporal decorrelation, see Zebker and Villasenor (1992).

Many of these issues have been addressed to an acceptable degree. Tropospheric moisture and its contribution to phase, known as atmospheric phase screening (APS), have been studied extensively, e.g. Hanssen (2001, Chapter 6), and Ferretti et al. (1999, Section 2), and a number of methods to address APS, without using external inputs like weather models, have been presented (Murray et al., 2019; Yu et al., 2017; Tymofyeyeva and Fialko, 2015). Absent real-time models of tropospheric moisture, one can assume APS varies slowly in space and any spatial variations in APS can be assumed to be uncorrelated between revisits (Zebker et al., 1997). This allows one to separate a deformation signal that is consistent in time from APS. Ionospheric effects, which tend to be more significant for L-band and longer wavelength systems, have been similarly studied (Chen and Zebker, 2013; Fattahi et al., 2017; Liang et al., 2019). Geometrical decorrelation has been largely addressed by better orbit control. Errors in DEMs manifest as a phase contribution that correlates with the component of orbit offsets that is perpendicular to the look direction. This effect is sufficiently reliable to use InSAR to generate DEMs (Van Zyl, 2001; Zink et al., 2014).

Assessments of the phase contribution due to changes in scattering properties have largely focused on how to select ”good” pixels to include in an InSAR analysis, e.g. Ferretti et al. (2001). The phase of any single pixel changes significantly between successive collections. This remains true even after removing the estimated phase contribution associated with the round trip distance, since, as noted above, the combined uncertainty in the orbit data and DEM exceeds half a wavelength. This inability to access the ”phase on the ground” can been addressed in several ways. In Ferretti et al. (2001) the authors present an elegant argument relating phase noise to temporal variations in amplitude, which is not affected by APS or orbit variation. This allows one to identify likely permanent scatterers (PS), i.e. pixels where scattering is dominated by a single stable feature. These PS pixels are included in the InSAR analysis. The drawback to this method is that it often selects too few pixels outside of urban areas. Indeed, the method presented in Ferretti et al. (2001) includes additional steps

Preprints (www.preprints.org) | NOT PEER-REVIEWED | Posted: 17 June 2022 doi:10.20944/preprints202206.0251.v1

to include more pixels that are consistent with the initial PS pixels, but which themselves do not have the desired amplitude statistics. Alternatively, because many pervasive phase contributions vary slowly in space, one can choose a spatial window to determine if the phase changes are at least consistent within that spatial window. At the simplest level one can estimate the interferometric phase difference between two SAR collections as shown in Eqs. 1.13 and 1.14 in Ferretti et al. (2007a). Here one approximates the expectation value of the phase change for pixel (Eq. 1.13) by assuming the statistics are sufficiently uniform within the averaging window (Eq. 1.14). There are more sophisticated methods that incorporate a stack of coregistered complex SAR images to estimate a consistent time series for the phase, e.g. Guarnieri and Tebaldini (2008); Ansari et al. (2018). We refer to phase quality between two SAR collections as *coherence*, and the phase quality for a stack of (more than two) SAR collections *temporal coherence*. These methods to estimate the quality of interferometric phase, and, in the cases of Ferretti et al. (2007a, Eq. 1.14), Guarnieri and Tebaldini (2008), and Ansari et al. (2018), the phase itself, are based on the idea that phase noise should be considered as a statistical process and these methods can estimate the parameters of that process.

These coherence estimation methods can also be used to estimate uncertainty in phase (Bamler and Just, 1993; Jong-Sen Lee et al., 1994, Figs. 2,3). One could assume that uncertainty in the wrapped phase is the same as the uncertainty in the unwrapped phase, and finally, accumulate uncertainty according to the chosen interfergram network. While this approach can give a rough approximation, there are two shortcomings worth noting. First, unwrapping is necessarily non-linear, and the uncertainty in the unwrapped phase will likely not be the same as the uncertainty in the wrapped phase. As an aside, it is the authors' experience that the iterative and conditional logic in unwrapping schemes makes

Preprints (www.preprints.org) | NOT PEER-REVIEWED | Posted: 17 June 2022 doi:10.20944/preprints202206.0251.v1

a naïve error propagation infeasible. Second, the historical uncertainty is often correlated in a manner that cannot be captured by a single number such as temporal coherence, or even by coherence between, say, successive SAR scenes. For example, coherence between fall and spring SAR scenes may be high, while snow causes scene-to-scene coherence involving scenes collected in winter months to be low. Indeed, *phase-linking* InSAR methods (cf. Guarnieri and Tebaldini (2008); Ansari et al. (2018)) use a sample correlation matrix (SCM) to reconstruct a consistent wrapped phase from all $N(N-1)/2$ non-redundant interferometric pairs. This suggests that models of uncertainties should capture correlations in those uncertainties.

This current work proposes a novel method to estimate uncertainty, more specifically precision, in deformation results based on uncertainty in phase on a point-by-point basis. The method is described in detail in Section 3. The two main ideas behind this method are, 1, we create synthetic data whose statistics match the statistics of the input data, then, 2, estimate the uncertainty based on the standard deviation of an ensemble calculation using these synthetic data. This method can then assess any deformation retrieval method by measuring the spread in results in the ensemble of deformations retrieved, and can allow the estimation of uncertainty between any two test and reference points. We demonstrate this with an example from a mining site in South Africa in Section 4.

2. Background

Previous studies have attempted to assess the accuracy of InSAR derived deformation using GPS/GNSS data, e.g. Ferretti et al. (2007b); Zebker (2021); Lee et al. (2005); Jiang and Lohman (2021); Armaş et al. (2016), leveling measurements, e.g. Yang et al. (2016); Marinkovic et al. (2007); Luo et al. (2017), or indirect methods such as water level, e.g. Wdowinski et al. (2004); Lu and Kwoun (2008) or precipitation, e.g. Palomino-Ángel et al. (2022). However, some of these methods cannot provide a direct comparison to deformation signals and therefore make it difficult to estimate accuracy or precision, and the uncertainty of other methods such as GPS/GNSS and leveling data are comparable if not greater than what is anticipated for InSAR measurements, e.g. You (2006). Further, these sources of validation are often temporally or spatially sparse, which does not allow one to estimate the accuracy of all points or epochs used in the InSAR surface deformation measurement and limits the ability to detect where the signal is most reliable and where it may be less accurate. Simulation has been used to assess particular phase contributions, e.g. Yunjun et al. (2019) provides a means to simulate atmospheric phase errors.

The method presented here is most similar to Agram and Simons (2015) where the authors present a thorough model of the correlations in uncertainties. The matrix that describes these correlations is quite large, and the current work does not so much "build on" but "remove from" that work, with the goal of establishing a more computational tractible method.

3. Method

3.1. Overview

Let N denote the number of complex SAR scenes. We choose a kernel k in the spatial domain and compute the Sample Correlation Matrix (SCM) for each pixel. Recall the r, c entry for the SCM (associated with time epochs r and c) corresponding to pixel i is

$$SCM^i_{rc} = \frac{\langle d^i_r ; d^i_c \rangle_k}{\|d^i_r\|_k \|d^i_c\|_k}. \tag{1}$$

where

- d_a^b is the co-registered complex SAR data at epoch a for pixel b,
- $\langle f; g \rangle_k$ is the inner product generated by integrating the convolution of the product $f\overline{g}$ with the kernel k and
- $\| \cdot \|_k$ is the induced L^2 norm, i.e. $\sqrt{\langle \cdot ; \cdot \rangle_k}$.

To generate sample data for pixel i, we notionally draw ϕ_0 from $(SCM^i)^{1/2}Z$ where Z is a random column-vector variable of N i.i.d. entries each drawn from the complex normal distribution $\mathcal{CN}(0,1)$. We let

$$\phi = \phi_0/|\phi_0|, \tag{2}$$

which we treat as the synthetic phase. The synthetic data for pixel i is then the Hadamard or element-wise product of amplitude vector of the input SAR data at pixel i and ϕ.

In addition to stacks of coregistered complex SAR scenes, InSAR analysis pipelines require a number of ancillary data such as orbit data and collection dates. We use these data from the input stack. With this, we can create an ensemble of synthetic data that have the same form as the input data, and any InSAR analytic pipeline can run on both real and synthetic data without change.

Running an InSAR analysis pipeline on an ensemble of such stacks generates a range of deformation results, which helps us understand the likely spread of deformation results due to decorrelation, and provides an estimate of precision per pixel and epoch.

3.2. Properties

There are a number properties of this method worth discussing.

The SCM may not be positive semidefinite. Since the SCM is Hermitian, we compute $(SCM^i)^{1/2}$ using an eigenvalue decomposition, taking the square roots of the eigenvalues. If we encounter any negative eigenvalues we set them to zero and proceed.

The phase of the SCM is reflected in the synthetic data. To see this we consider the case of the SCM for a pixel for two epochs. The SCM will have the following form

$$SCM = \begin{bmatrix} 1 & z \\ z^* & 1 \end{bmatrix}, \tag{3}$$

where the modulus of z is the coherence and the argument of z is the estimated interferometric phase, both of which will depend on our choice of kernel. The eigenvalues and corresponding eigenvectors are $1+|z|$, $\frac{1}{\sqrt{2}}[\exp(i\theta), 1]^T$ and $1-|z|$, $\frac{1}{\sqrt{2}}[-\exp(i\theta), 1]^T$, where θ is chosen such that $\exp(i\theta) = \frac{z}{|z|}$. We can compute the square root of the SCM as

$$SCM^{1/2} = \frac{1}{2} \begin{bmatrix} U & V\exp(i\theta) \\ V\exp(-i\theta) & U \end{bmatrix}, \tag{4}$$

where

- $U = \sqrt{1+|z|} + \sqrt{1-|z|}$ and
- $V = \sqrt{1+|z|} - \sqrt{1-|z|}$.

For two i.i.d. random complex Gaussian variables Z_1 and Z_2, we can compute the synthetic phase at the two epochs as

$$\begin{pmatrix} P_1 \\ P_2 \end{pmatrix} \equiv SCM^{1/2} \begin{pmatrix} Z_1 \\ Z_2 \end{pmatrix} = \frac{1}{2} \begin{pmatrix} UZ_1 + V\exp(i\theta)Z_2 \\ V\exp(-i\theta)Z_1 + UZ_2 \end{pmatrix} \tag{5}$$

We are interested in the relative phase of P_1 and P_2 so we consider

$$
\begin{aligned}
P_1\overline{P_2} = \tfrac{1}{4}\exp(i\theta)(& \\
& UV|Z_1|^2 \\
& +U^2 Z_1 \overline{Z_2} \exp(-i\theta) \\
& +V^2 Z_2 \overline{Z_1} \exp(i\theta) \\
& +UV|Z_2|^2 \\
)&
\end{aligned}
\tag{6}
$$

The expectation value of this is

$$\frac{1}{2}|z|\mathbb{E}(|Z_1|^2)\exp(i\theta), \tag{7}$$

and has phase θ. The standard deviation of the phase of $P_1\overline{P_2}$ as a function of $\gamma = |z|$ derived from numerical experiment is shown in Figure 1, and has the expected form (Bamler and Just, 1993).

For this reason, phase contributions from sources whose length scales exceed the width of k – typically APS, deformation and gross DEM errors – will be reproduced in the synthetic data (Guarnieri and Tebaldini, 2007), and one should not add these phase contributions in via additional simulated data.

We are using the SCM as a covariance matrix. It is natural to consider using the covariance matrix itself, which will only fail to be Hermitian positive semi-definite in the case of roundoff error. The covariance matrix would be appropriate if we were attempting to estimate the uncertainty in, and create synthetic versions of, both the amplitude and phase by using a windowed average specified by k. Our goal, however, is to create synthetic data that allows us to

Preprints (www.preprints.org) | NOT PEER-REVIEWED | Posted: 17 June 2022 doi:10.20944/preprints202206.0251.v1

estimate the uncertainty in phase estimations obtained by spatial averaging.[1].

One must choose k. The choice of k impacts the effective resolution of the synthetic data. One should choose k large enough to capture the uncertainty, but small enough to resolve the features of interest.

Such synthetic data are only appropriate for kernel-based phase estimation. This process of generating synthetic data assumes that phase statistics are nearly uniform on a small scale, and that the kernel k can recover these phase statistics.

This assumption does not hold for a single permanent scatterer surrounded by noisy pixels. Consequently, if one uses amplitude dispersion to detect PSs within a noisy surrounding environment, these synthetic data will not represent the uncertainty in the phase recovered from pixels selected by amplitude dispersion. The method we propose here will construct synthetic data using the statistics from a windowed average, the synthetic version of a single PS surrounded by noisy pixels will reflect the entire neighborhood of that PS, and will not capture the quality of that single pixel on its own. Note that, because the synthetic data uses the original amplitudes, the amplitude dispersion calculation will agree exactly for both synthetic and real data, while the synthetic phase for the pixel will likely be less reliable than the corresponding real phase.

One can create synthetic data for single pixels, essentially following Ferretti et al. (2001). One creates a Rice distribution that matches the observed amplitude dispersion, selects the phase from the samples and pairs that with the input amplitude. While substantially simpler than our method based on the SCM, it suffers the drawback that the phase statistics are assumed to be fixed in time, as the estimate] is parametrized by a single input statistic. In this case, e.g., seasonal noise will not be captured. Further, such a method will, without

[1]We attempted to use the actual covariance matrix and found that the resulting synthetic data had coherence that was much lower than the coherence of the real data.

additional inputs, produce synthetic data with mean zero phase.

4. Example

As an example, we apply our analytic methods to a mining operation in South Africa, shown in Figure 2. We use a stack of 31 images collected by Sentinel-1 track 131 between November of 2019 and November of 2020. The images were coregistered to a UTM grid with resolution of 2.5m East-West by 10m North-South. We chose the anisotropic resolution of the UTM grid to approximate the anisotropy of range and azimuth resolutions in an IW-TOPS mode collection.

We compare coherence between two scenes (Figure 3) and the magnitude of the SCM for an arbitrary pixel (Figure 4) derived from real data and synthetic data. In both cases it is evident that the coherence for the real data is slightly higher than it is for the synthetic data. We show this descrepency in Figure 5. This plot shows the absolute values of SCM entries for synthetic data plotted against the absolute value for corresponding entries for real data. We've binned the data into narrow intervals of real coherence and computed the standard deviation of the synthetic coherence.

There are two notable features in Figure 5. First, the largest difference between coherence of real and synthetic data occurs roughly when the coherence of the real data is 0.7. At this point the coherence of the synthetic data has a mean of 0.56. Our hypothesis is that our noise model fails to capture correlations between nearby pixels that increase coherence. Second, at very low coherence the synthetic coherence is higher than real coherence. We believe this is caused partly because noise perturbes the SCM from being purely diagonal, but primarily because the coherence is bounded below by zero, and the mean is likely not entirely appropriate for determining a "representative" synthetic coherence.

We anticipate that the first issue – that our model fails to capture correlations between nearby pixels – will have two effects. First, we believe that ensemble studies will likely overestimate the uncertainties, and second we might see systematic biases in the mean of the ensemble results. For this reason, we use ensemble results primarily as a tool to estimate uncertainties in particular deformation retrieval methods, and take that as a likely upper bound on the uncertanty.

We apply our ensemble methods to two deformation retrieval methods. The first, which we will call method 1, begins by using a variant of the recursive phase estimation scheme described in Ansari et al. (2018). Pixels are included based on temporal coherence, in particular the ability to find a rank-one approximation of the SCM per ministack. We then form a mesh of all spatial links less than a certain radius. For each link we apply the LAMBDA method described in Kampes and Hanssen (2004), rejecting links based on their temporal coherence. We reconstruct point data from link data using the method described in Gonzalez et al. (2011). The second method (method 2) estimates phase using the *phase-linking* method described in Guarnieri and Tebaldini (2008). As with the first method, pixels are include based on temporal coherence. Following Pepe and Lanari (2006), we use a minimum cost-flow method to establish consistent link values in temporal-perpendicular baseline-space, and then use a minimum cost-flow method on the Delaunay triangulation of good points to recover unwrapped phase per point. With both methods we look for historically anomalous jumps of 2π, which we treat as unwrapping errors and attempt to remove. No effort has been made to identify and remove APS, nor have we applied any temporal smoothing.

We've run each method on the real data, and on an ensemble of thirty syn-

Preprints (www.preprints.org) | NOT PEER-REVIEWED | Posted: 17 June 2022 doi:10.20944/preprints202206.0251.v1

thetic stacks of data. These sixty-two deformation retrieval computations were performed on the Descartes Labs Platform (Beneke et al., 2017). Deformation histories for the test points relative to the reference point, as shown in Figure 2, are presented in Figures 6, 7, 8 and 9. The orange crosses in these figures show deformation histories derived only from actual complex SAR data, while the blue circles with error bars show the ensemble mean and standard deviation of deformation histories derived only from synthetic data.

In Figures 6 and 7 the deformation at the green point relative to the orange point retrieved by the two methods from the actual data (orange crosses) are largely in agreement. The standard deviations of the ensemble results (blue dots and error bars) for method 1 are smaller than those of method 2, suggesting that *for this pair of test and reference points* method 1 is less sensitive to phase noise.

In Figure 8 the deformation at the blue point relative to the orange point retrieved from the actual data by method 1 (orange crosses) suggests almost no deformation, however the ensemble mean standard deviation (blue dots and error bars) suggest that this method *for this pair of test and reference points* is very sensitive to the modeled phase noise. In Figure 9 method 2 shows roughly $50mm$ of deformation and *for this pair of test and reference points* is not nearly so sensitive to phase noise.

5. Discussion

InSAR results can vary based on the deformation retrieval method, e.g. (Hu et al., 2016; Osmanoğlu et al., 2016; Parizzi and Brcic, 2010; Yang et al., 2016, Figs. 8,9), and even individual methods likely have accuracy and uncertainty that varies in space and time. This can make it difficult to determine which points in the results are actually reliable, or to determine the best deformation retrieval method to use for a particular area of interest.

The primary value in this ensemble calculation is that it allows us to determine the method that is least sensitive to phase noise and therefore the best method to choose for a particular set of points or area of interest. For instance, we see that the estimated uncertainty is relatively small for the green test point relative to the orange reference point for both method 1 and 2, and while method 1 may be less sensitive to phase noise, both methods have uncertainties within the range we can expect for InSAR measurements (Rosen et al., 2000). However, the relative uncertainty between the blue test point and the orange reference point for method 1 is quite high, indicating this method is very sensitive to phase noise for this test and reference pair combination, and therefore would not be the best deformation retrieval method to choose for recovering relative deformation between this pair of points.

The other main benefit in using the presented approach is that, because this method estimates uncertainty point-by-point and epoch-by-epch, one can filter points based on the magnitude of their estimated uncertainty, which allows confidence that the extracted deformation at the remaining points is likely insensitive to phase noise and is likely more reliable. In the above example, if method 1 was selected and the orange point chosen as our reference, we would exclude the blue test point due to its high sensitivity to the modeled phase noise, but would preserve the green test point due to its lower uncertainty.

As we can see in the second-to-last epoch of Figures 6 and 7, there are likely other sources of phase changes beyond expected deformation and estimated phase noise. These other sources add temporal "jitter" to the signal that exceeds the standard deviations. This "jitter" is correlated between the methods, and is captured in both the ensemble mean and the actual retrieved deformation. Further, the standard deviation doesn't grow in time at these events. From this we conclude that this jitter is caused by some other physical phase contribution, possibly APS or maybe spatially varying dielectric changes in the surface in response to other environmental effects.

As we discussed in Section 3, we treat a correlation matrix as a covariance matrix, and take the square root of positive semi-definite approximation of this correlation matrix. While these approximations may not be entirely accurate, they appear to best match the real coherence data, and enable us to acheive beneficial insights into the reliability of each point we analyze. However, this method does not perfectly capture coherence using the correlation matrix, which may cause us to over estimate our uncertainty in some cases, so we take the standard deviation of the spread as the upper bound on the uncertainty.

As for the computational and storage costs, aside from generating the synthetic data, we must run the entire deformation retrieval process tens of times to generate the actual retrieved deformation and the ensemble analysis, which can each be computationally-expensive, depending on the size and resolution of the area. We also must store each of these results before actually calculating the ensemble mean and standard deviation, which adds additional storage and computation costs. Because the standard deviations varies with choice of reference point, there is not a way to compute the standard deviation "up front". Instead, when reviewing the results, we have all ensemble results available and re-compute the standard deviations for the test point if we move the reference point. Although this does add some additional computation and storage costs, it also allows for the flexibility assess the best reference point, and to compare relative differences in standard deviation for points that are near to each other spatially, which can help eliminate noisy points.

6. Conclusions

We've developed a method for generating synthetic SAR data stacks based on real SAR data stacks. The coherence and estimated phase statistics of the synthetic data appears to match those same properties of the real data. This allows us to perform ensemble studies to assess the sensitivity of particular deformation retrieval method to phase noise. The proposed ensemble analysis can provide a point-by-point, epoch-by-epoch, indication of reliability of the result.

Futher research includes a more thorough understanding of possible biases in the simulated synthetic phase.

7. Acknowledgements

The authors would like to thank Mike Warren and Scott Arko for maintaining Descartes Labs Sentinel-1 data pipeline and for helpful discussions relating to InSAR. This work contains modified Copernicus Sentinel data 2019-2020, processed by ESA.

References

Agram, P.S., Simons, M., 2015. A noise model for insar time series. Journal of Geophysical Research: Solid Earth 120, 2752–2771. doi:10.1002/2014JB011271.

Ansari, H., De Zan, F., Bamler, R., 2018. Efficient phase estimation for interferogram stacks. IEEE Transactions on Geoscience and Remote Sensing 56, 4109–4125.

Preprints (www.preprints.org) | NOT PEER-REVIEWED | Posted: 17 June 2022 doi:10.20944/preprints202206.0251.v1

Armaş, I., Gheorghe, M., Lendvai, A.M., Dumitru, P.D., Bădescu, O., Călin, A., 2016. Insar validation based on gnss measurements in bucharest. International Journal of Remote Sensing 37, 5565–5580.

Bamler, R., Just, D., 1993. Phase statistics and decorrelation in sar interferograms, in: Proceedings of IGARSS'93-IEEE International Geoscience and Remote Sensing Symposium, IEEE. pp. 980–984.

Beneke, C.M., Skillman, S., Warren, M.S., Kelton, T., Brumby, S.P., Chartrand, R., Mathis, M., 2017. A platform for scalable satellite and geospatial data analysis, in: AGU Fall Meeting Abstracts, pp. IN32C–04.

Berardino, P., Fornaro, G., Lanari, R., Sansosti, E., 2002. A new algorithm for surface deformation monitoring based on small baseline differential sar interferograms. IEEE Transactions on Geoscience and Remote Sensing 40, 2375–2383.

Chen, A.C., Zebker, H.A., 2013. Reducing ionospheric effects in insar data using accurate coregistration. IEEE transactions on geoscience and remote sensing 52, 60–70.

Fattahi, H., Simons, M., Agram, P., 2017. Insar time-series estimation of the ionospheric phase delay: An extension of the split range-spectrum technique. IEEE Transactions on Geoscience and Remote Sensing 55, 5984–5996.

Ferretti, A., Monti-Guarnieri, A., Prati, C., Rocca, F., 2007a. Part c insar processing: a mathematical approach. InSAR Principles: Guidelines for SAR Interferometry Procs. and Interpretation, K. Fletcher, Ed., ESA Publications: Noordwijk, Netherlands , 3–13.

Ferretti, A., Prati, C., Rocca, F., 1999. Multibaseline insar dem reconstruction:

 doi:10.20944/preprints202206.0251.v1

The wavelet approach. IEEE Transactions on geoscience and remote sensing 37, 705–715.

Ferretti, A., Prati, C., Rocca, F., 2001. Permanent scatterers in sar interferometry. IEEE Transactions on Geoscience and Remote Sensing 39, 8–20.

Ferretti, A., Savio, G., Barzaghi, R., Borghi, A., Musazzi, S., Novali, F., Prati, C., Rocca, F., 2007b. Submillimeter accuracy of insar time series: Experimental validation. IEEE Transactions on Geoscience and Remote Sensing 45, 1142–1153.

Goldstein, R., 1995. Atmospheric limitations to repeat-track radar interferometry. Geophysical research letters 22, 2517–2520.

Goldstein, R.M., Zebker, H.A., Werner, C.L., 1988. Satellite radar interferometry: Two-dimensional phase unwrapping. Radio science 23, 713–720.

Gonzalez, F.R., Bhutani, A., Adam, N., 2011. L1 network inversion for robust outlier rejection in persistent scatterer interferometry, in: 2011 IEEE International Geoscience and Remote Sensing Symposium, IEEE. pp. 75–78.

Guarnieri, A.M., Tebaldini, S., 2007. Hybrid cramér–rao bounds for crustal displacement field estimators in sar interferometry. IEEE signal processing letters 14, 1012–1015.

Guarnieri, A.M., Tebaldini, S., 2008. On the exploitation of target statistics for sar interferometry applications. IEEE Transactions on Geoscience and Remote Sensing 46, 3436–3443.

Hanssen, R.F., 2001. Radar interferometry: data interpretation and error analysis. volume 2. Springer Science & Business Media.

Hu, J., Ding, X., Li, Z., Zhang, L., Zhu, J., Sun, Q., Gao, G., 2016. Vertical and horizontal displacements of los angeles from insar and gps time series analysis:

Resolving tectonic and anthropogenic motions. Journal of Geodynamics 99, 27–38.

Jiang, J., Lohman, R.B., 2021. Coherence-guided insar deformation analysis in the presence of ongoing land surface changes in the imperial valley, california. Remote Sensing of Environment 253, 112160.

Jong-Sen Lee, Hoppel, K.W., Mango, S.A., Miller, A.R., 1994. Intensity and phase statistics of multilook polarimetric and interferometric sar imagery. IEEE Transactions on Geoscience and Remote Sensing 32, 1017–1028.

Kampes, B.M., Hanssen, R.F., 2004. Ambiguity resolution for permanent scatterer interferometry. IEEE Transactions on Geoscience and Remote Sensing 42, 2446–2453.

Lee, I., Chang, H.C., Ge, L., 2005. Gps campaigns for validation of insar derived dems. Journal of Global Positioning Systems 4, 82–87.

Liang, C., Agram, P., Simons, M., Fielding, E.J., 2019. Ionospheric correction of insar time series analysis of c-band sentinel-1 tops data. IEEE Transactions on Geoscience and Remote Sensing 57, 6755–6773.

Lu, Z., Kwoun, O.i., 2008. Radarsat-1 and ers insar analysis over southeastern coastal louisiana: Implications for mapping water-level changes beneath swamp forests. IEEE Transactions on Geoscience and Remote Sensing 46, 2167–2184.

Luo, Q., Zhou, G., Perissin, D., 2017. Monitoring of subsidence along jingjin inter-city railway with high-resolution terrasar-x mt-insar analysis. Remote Sensing 9, 717.

Marinkovic, P., Ketelaar, G., van Leijen, F., Hanssen, R., 2007. Insar quality

Preprints (www.preprints.org) | NOT PEER-REVIEWED | Posted: 17 June 2022 doi:10.20944/preprints202206.0251.v1

control: Analysis of five years of corner reflector time series, in: Proceedings of Fringe 2007 Workshop (ESA SP-649), Frascati, Italy, p. 30.

Murray, K.D., Bekaert, D.P., Lohman, R.B., 2019. Tropospheric corrections for insar: Statistical assessments and applications to the central united states and mexico. Remote Sensing of Environment 232, 111326.

Osmanoğlu, B., Sunar, F., Wdowinski, S., Cabral-Cano, E., 2016. Time series analysis of insar data: Methods and trends. ISPRS Journal of Photogrammetry and Remote Sensing 115, 90–102.

Palomino-Ángel, S., Vázquez, R., Hampel, H., Anaya, J., Mosquera, P., Lyon, S.W., Jaramillo, F., 2022. Retrieval of simultaneous water-level changes in small lakes with insar. Geophysical Research Letters 49, e2021GL095950.

Parizzi, A., Brcic, R., 2010. Adaptive insar stack multilooking exploiting amplitude statistics: A comparison between different techniques and practical results. IEEE Geoscience and Remote Sensing Letters 8, 441–445.

Pepe, A., Lanari, R., 2006. On the extension of the minimum cost flow algorithm for phase unwrapping of multitemporal differential sar interferograms. IEEE Transactions on Geoscience and remote sensing 44, 2374–2383.

Rodriguez, E., Martin, J., 1992. Theory and design of interferometric synthetic aperture radars, in: IEE Proceedings F (Radar and Signal Processing), IET. pp. 147–159.

Rosen, P.A., Hensley, S., Joughin, I.R., Li, F.K., Madsen, S.N., Rodriguez, E., Goldstein, R.M., 2000. Synthetic aperture radar interferometry. Proceedings of the IEEE 88, 333–382.

Tymofyeyeva, E., Fialko, Y., 2015. Mitigation of atmospheric phase delays in insar data, with application to the eastern california shear zone. Journal of Geophysical Research: Solid Earth 120, 5952–5963.

Van Zyl, J.J., 2001. The shuttle radar topography mission (srtm): a breakthrough in remote sensing of topography. Acta Astronautica 48, 559–565.

Wdowinski, S., Amelung, F., Miralles-Wilhelm, F., Dixon, T.H., Carande, R., 2004. Space-based measurements of sheet-flow characteristics in the everglades wetland, florida. Geophysical Research Letters 31.

Yang, K., Yan, L., Huang, G., Chen, C., Wu, Z., 2016. Monitoring building deformation with insar: Experiments and validation. Sensors 16, 2182.

You, R.J., 2006. Local geoid improvement using gps and leveling data: Case study. Journal of surveying engineering 132, 101–107.

Yu, C., Penna, N.T., Li, Z., 2017. Generation of real-time mode high-resolution water vapor fields from gps observations. Journal of Geophysical Research: Atmospheres 122, 2008–2025.

Yunjun, Z., Fattahi, H., Amelung, F., 2019. Small baseline insar time series analysis: Unwrapping error correction and noise reduction. Computers and Geosciences 133, 104331.

Zebker, H., 2021. Accuracy of a model-free algorithm for temporal insar tropospheric correction. Remote Sensing 13, 409.

Zebker, H.A., Rosen, P.A., Hensley, S., 1997. Atmospheric effects in interferometric synthetic aperture radar surface deformation and topographic maps. Journal of geophysical research: solid earth 102, 7547–7563.

Zebker, H.A., Villasenor, J., 1992. Decorrelation in interferometric radar echoes. IEEE Transactions on geoscience and remote sensing 30, 950–959.

Zink, M., Bachmann, M., Brautigam, B., Fritz, T., Hajnsek, I., Moreira, A., Wessel, B., Krieger, G., 2014. Tandem-x: The new global dem takes shape. IEEE Geoscience and Remote Sensing Magazine 2, 8–23.

List of Figures

 doi:10.20944/preprints202206.0251.v1

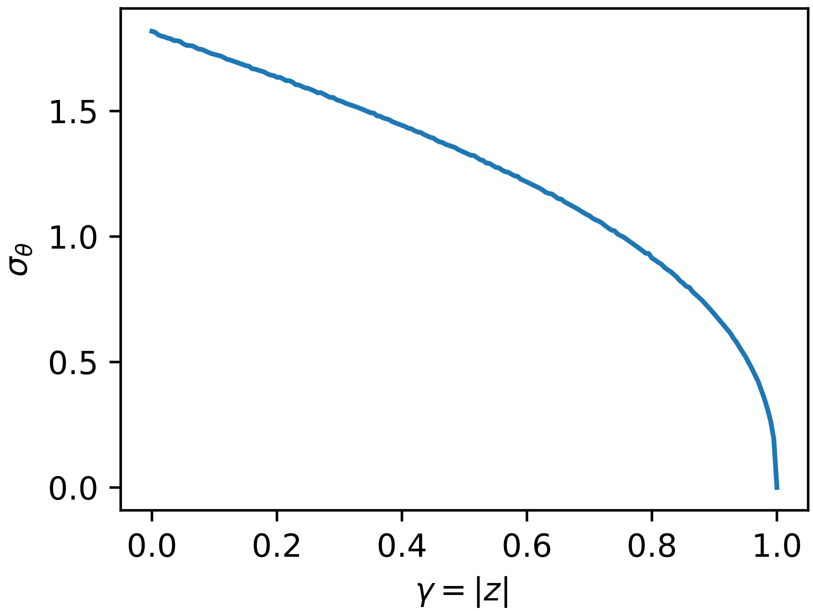

Figure 1: Numerical experiments showing the standard deviation of phase of $P_1\overline{P_2}$ as a function of $\gamma = |z|$.

Preprints (www.preprints.org) | NOT PEER-REVIEWED | Posted: 17 June 2022 doi:10.20944/preprints202206.0251.v1

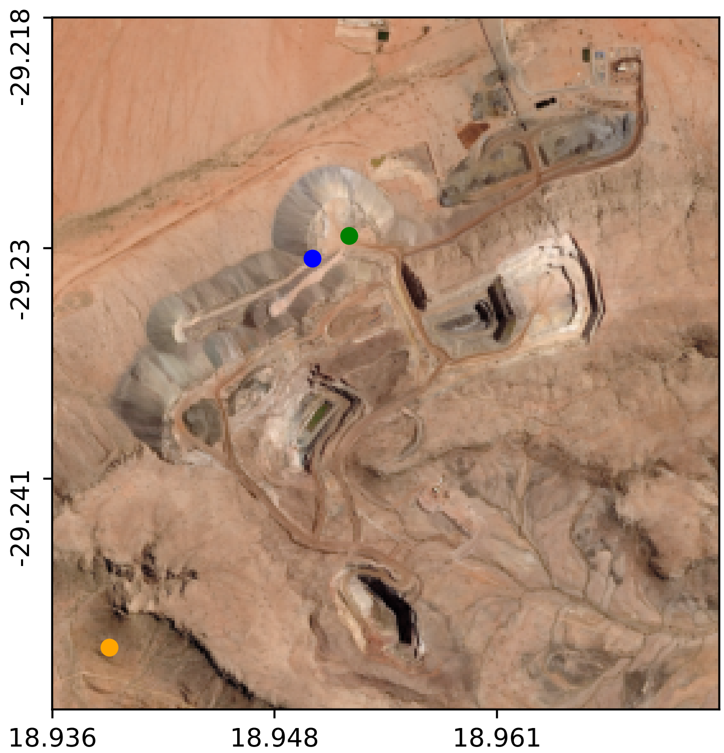

Figure 2: Our area of interest with the reference point (orange) and test points (green and blue).

doi:10.20944/preprints202206.0251.v1

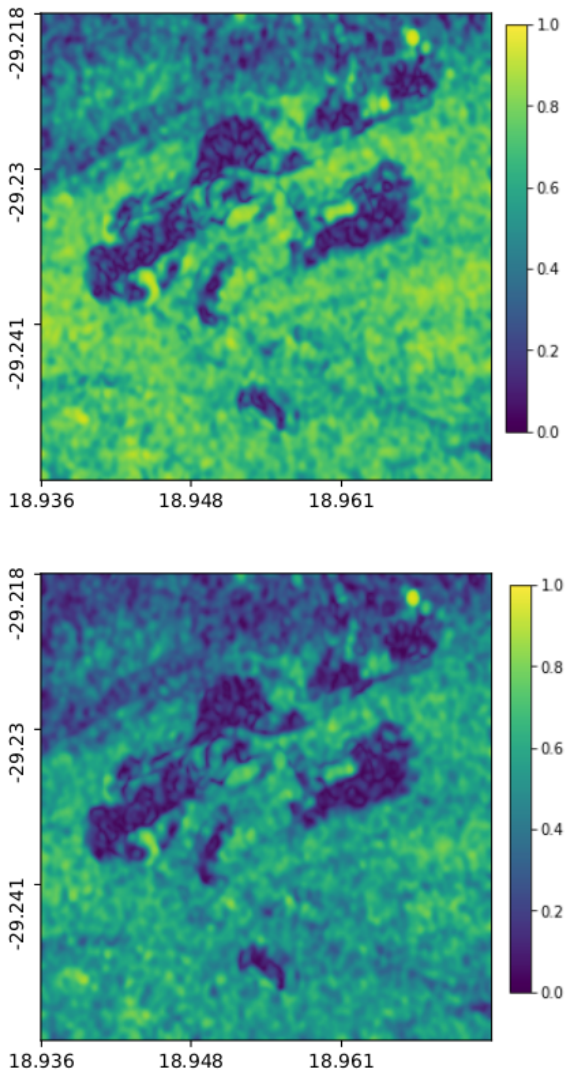

Figure 3: Coherence between the tenth and twentieth scene for real input data (top) and synthetic data (bottom).

Preprints (www.preprints.org) | NOT PEER-REVIEWED | Posted: 17 June 2022 doi:10.20944/preprints202206.0251.v1

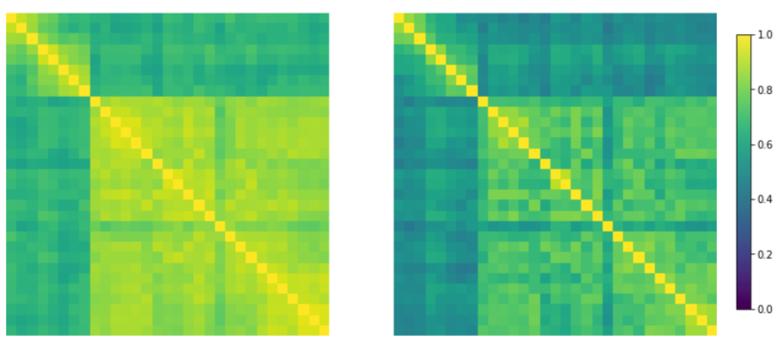

Figure 4: Absolute value of the sample correlation matrix for an arbitrary pixel using real data (left) and synthetic data (right).

Preprints (www.preprints.org) | NOT PEER-REVIEWED | Posted: 17 June 2022 doi:10.20944/preprints202206.0251.v1

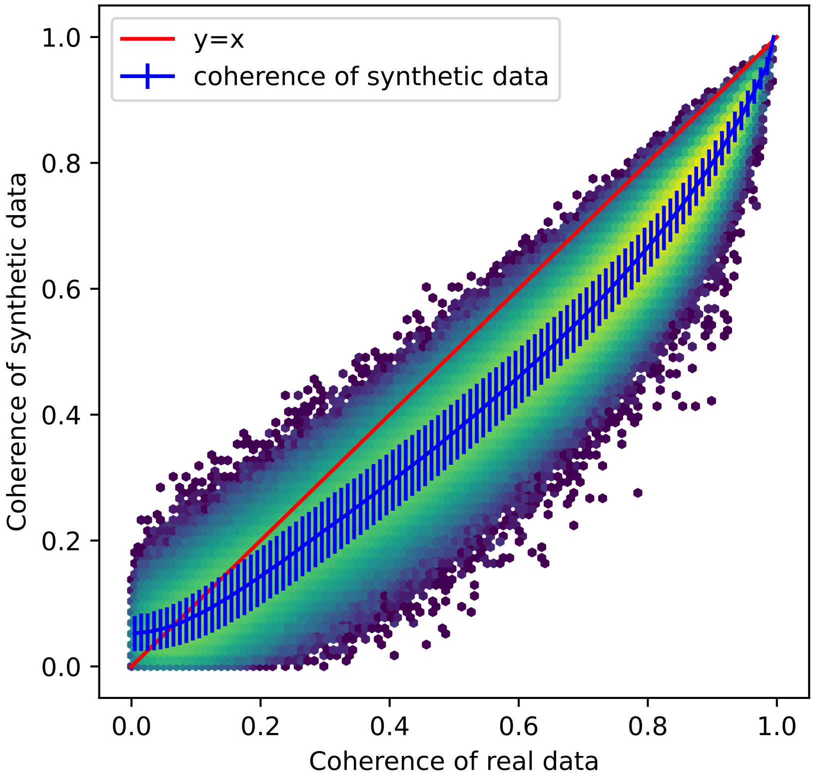

Figure 5: A heat plot of coherence from synthetic data vs. coherence from real data. The red line is $y = x$ and the blue line is the mean synthetic coherence, with an error bar showing the standard deviation of values.

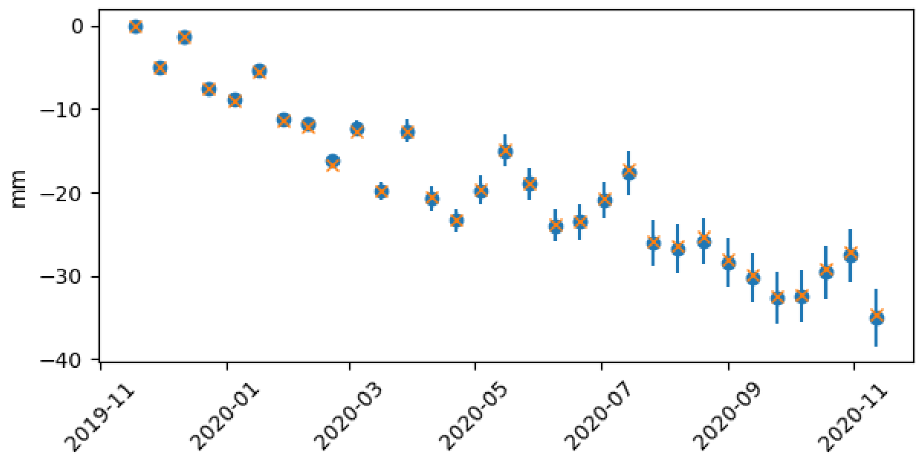

Figure 6: Recovered deformation histories of the green test point relative to the orange reference point as shown in Figure 2 for method 1.

Preprints (www.preprints.org) | NOT PEER-REVIEWED | Posted: 17 June 2022 doi:10.20944/preprints202206.0251.v1

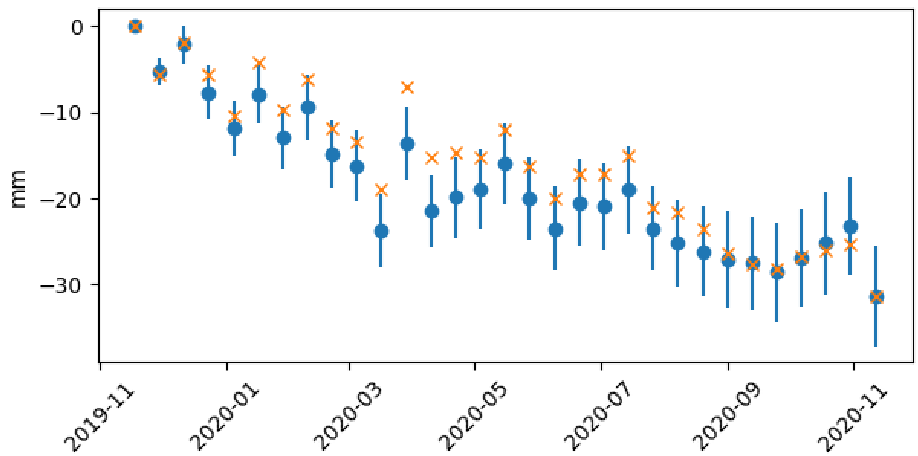

Figure 7: Recovered deformation histories of the green test point relative to the orange reference point as shown in Figure 2 for method 2.

Preprints (www.preprints.org) | NOT PEER-REVIEWED | Posted: 17 June 2022 doi:10.20944/preprints202206.0251.v1

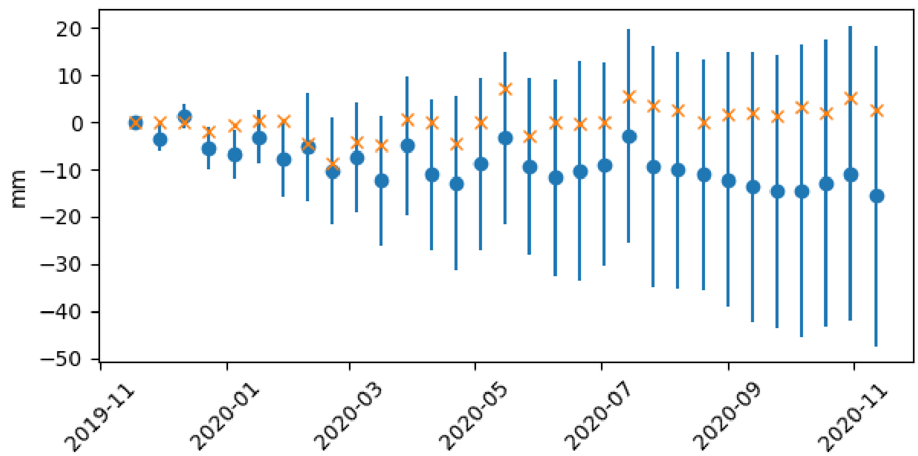

Figure 8: Recovered deformation histories of the blue test point relative to the orange reference point as shown in Figure 2 for method 1.

Preprints (www.preprints.org) | NOT PEER-REVIEWED | Posted: 17 June 2022 doi:10.20944/preprints202206.0251.v1

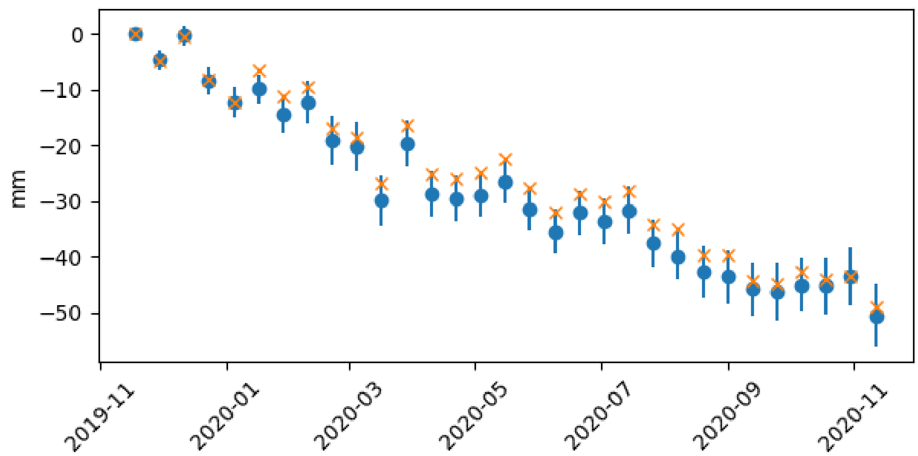

Figure 9: Recovered deformation histories of the blue test point relative to the orange reference point as shown in Figure 2 for method 2.